Cell Reports
Methods

Article

Large-scale interrogation of retinal cell functions by 1-photon light-sheet microscopy

Graphical abstract

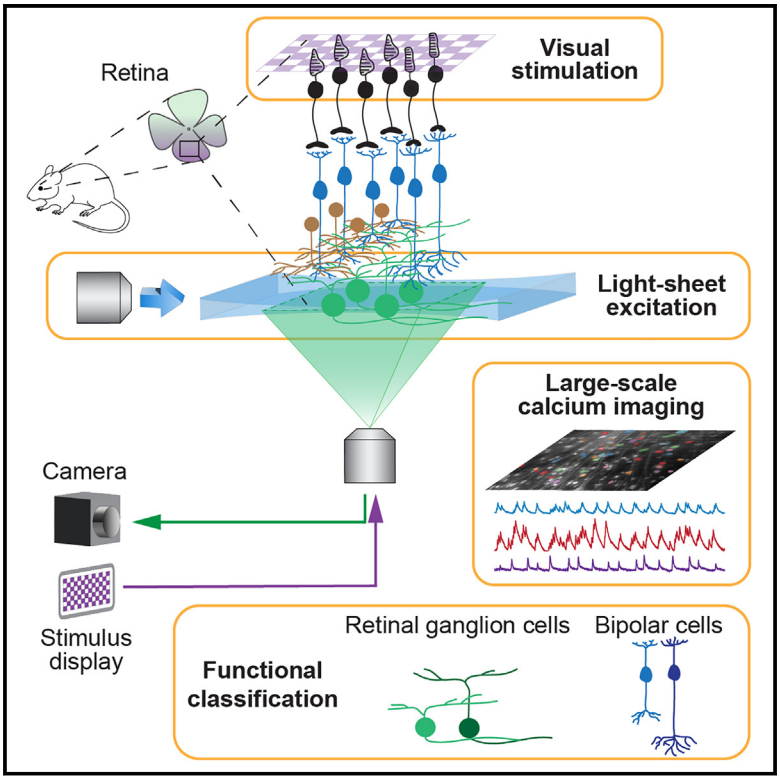

Authors

Suva Roy, Depeng Wang, Andra M. Rudzite, ..., Yiyang Gong, Alexander Sher, Greg D. Field

Correspondence

suva.roy@duke.edu

In brief

Roy et al. present a 1-photon-based light-sheet imaging system that allows monitoring of calcium activity in large populations of retinal neurons at synaptic resolution. This is an affordable, flexible, and high-throughput imaging platform that can be a useful tool for large-scale interrogation of functional connectivity between cell types in the retina.

Highlights

- 1-photon light-sheet imaging system for retinal studies
- The system is modular, high-throughput, and less expensive than 2-photon systems
- Allows calcium imaging of large neural population activity at synaptic resolution
- Allows functional classification of retinal ganglion cells and bipolar cells

Roy et al., 2023, Cell Reports Methods *3*, 100453
April 24, 2023
https://doi.org/10.1016/j.crmeth.2023.100453

CellPress

Cell Reports Methods

CellPress
OPEN ACCESS

Article

Large-scale interrogation of retinal cell functions by 1-photon light-sheet microscopy

Suva Roy,[1,6,*] Depeng Wang,[2,5] Andra M. Rudzite,[1] Benjamin Perry,[2] Miranda L. Scalabrino,[1,3] Mishek Thapa,[1,3] Yiyang Gong,[2] Alexander Sher,[4] and Greg D. Field[1,3]

[1]Department of Neurobiology, Duke University School of Medicine, Durham, NC 27710, USA
[2]Department of Biomedical Engineering, Duke University, Durham, NC 27708, USA
[3]Stein Eye Institute, Department of Ophthalmology, University of California, Los Angeles, Los Angeles, CA 90024, USA
[4]Santa Cruz Institute for Particle Physics, University of California, Santa Cruz, Santa Cruz, CA 95064, USA
[5]Present address: College of Energy and Power Engineering, Nanjing University of Aeronautics and Astronautics, Nanjing, China
[6]Lead contact
*Correspondence: suva.roy@duke.edu
https://doi.org/10.1016/j.crmeth.2023.100453

MOTIVATION Approximately 100 neuronal cell types comprise the mammalian retina. A central goal toward understanding early visual processing is to determine how signals flow through this network of cell types. To meet this goal, we developed a 1-photon light-sheet imaging system. This system allows for measuring the activity of hundreds of neurons simultaneously while presenting a visual stimulus. The system is also capable of resolving the activity of individual synapses and is much less expensive than competing 2-photon imaging systems. We anticipate this system will accelerate the understanding of retinal circuits and could be used to study other neural circuits under *ex vivo* conditions.

SUMMARY

Visual processing in the retina depends on the collective activity of large ensembles of neurons organized in different layers. Current techniques for measuring activity of layer-specific neural ensembles rely on expensive pulsed infrared lasers to drive 2-photon activation of calcium-dependent fluorescent reporters. We present a 1-photon light-sheet imaging system that can measure the activity in hundreds of neurons in the *ex vivo* retina over a large field of view while presenting visual stimuli. This allows for a reliable functional classification of different retinal cell types. We also demonstrate that the system has sufficient resolution to image calcium entry at individual synaptic release sites across the axon terminals of dozens of simultaneously imaged bipolar cells. The simple design, large field of view, and fast image acquisition make this a powerful system for high-throughput and high-resolution measurements of retinal processing at a fraction of the cost of alternative approaches.

INTRODUCTION

Imaging changes in the fluorescence of activity-dependent reporters targeted to genetically defined cell types have greatly expanded the kinds of measurements available in neuroscience. For example, imaging calcium-dependent fluorescence allows for measuring activity across hundreds to thousands of neurons simultaneously.[1,2] It also allows measuring signals at individual synapses and within subcellular compartments such as dendrites[3] without rupturing the cell membrane. However, fluorescence imaging relies on delivering large amounts of light to excite the fluorescent reporter. In the retina, this presents a problem because the excitation light will also drive phototransduction in rod and cone photoreceptors. To overcome this challenge, previous studies have relied on infrared 2-photon excitation of fluorescent reporters.[1,4,5] This greatly reduces, though does not eliminate, photoreceptor activation and allows imaging changes in fluorescence of downstream neurons while stimulating the photoreceptors in the visible spectrum.[6,7] A drawback of this approach is that it requires femtosecond pulsed infrared lasers, which are expensive to acquire and maintain.

We have developed a 1-photon light-sheet imaging system for *ex vivo* retinal measurements that has a simple setup and uses a much less expensive laser. The excitation light is restricted to a relatively expansive (2.25 mm^2) yet thin ($\sim$20 μm) plane, thus allowing hundreds of retinal neurons to be imaged

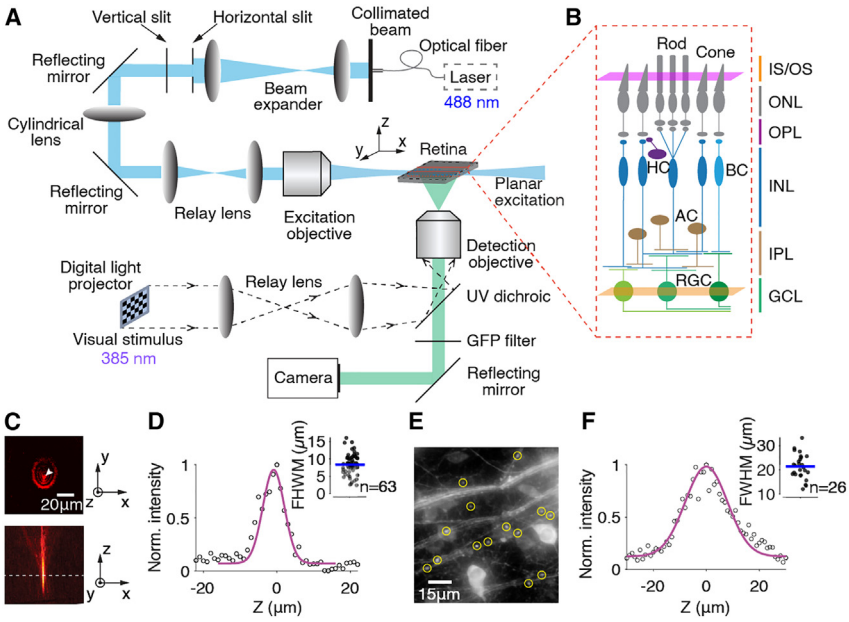

Figure 1. Design and characterization of a 1-photon light-sheet microscope for *ex vivo* retinal imaging

(A) Optical arrangement producing a Gaussian beam light sheet from a 488 nm continuous wave laser source. The light sheet is co-planar with the retinal imaging plane. The visual stimulus is projected onto the photoreceptors through a detection objective. A high-speed CMOS camera captured the fluorescence images.

(B) Schematized retinal circuit with stimulus plane (magenta) and imaging plane (orange). IS/OS, inner segment/outer segment of photoreceptors; ONL, outer nuclear layer; OPL, outer plexiform layer; INL, inner nuclear layer, IPL, inner plexiform layer; GCL, ganglion cell layer; HC, horizontal cell; BC, bipolar cell; AC, amacrine cell; RGC, retinal ganglion cell.

(C) Light-sheet imaging of fluorescent microspheres (500 nm diameter) using a 20× objective. Top: lateral image; bottom: axial image.

(D) Axial intensity profile of an imaged microsphere. Magenta curve: Gaussian fit. Inset: full-width half maximum (FWHM) of Gaussian fits for n = 63 microspheres. Depth of field = 8.5 ± 2.8 μm.

(E) GCaMP6f expression in varicosities (yellow circles) along RGC axons.

(F) Axial intensity profile of a representative varicosity (magenta curve) and depth of field, 22.2 ± 8.1 μm, estimated from n = 26 varicosities.

simultaneously and calcium signals to be resolved at the level of individual synapses. The system leverages the laminar organization of the retina: photoreceptors are in one cellular lamina, retinal interneurons are in a central lamina (containing horizontal, bipolar, and amacrine cells), and the retinal ganglion cell (RGC) layer forms a third cellular lamina (containing amacrine and ganglion cells). Between these layers of cell bodies, there are two synaptic laminae: the outer plexiform layer between photoreceptors and interneurons and the inner plexiform layer (IPL) between interneurons and RGCs.[8] The light sheet can be directed to a lamina not containing photoreceptors, thereby reducing photoreceptor activation. While a small fraction of the fluorescence excitation light does reach the photoreceptors, it is not efficiently absorbed by the mouse short-wavelength-sensitive opsin (S-opsin).[9] This opsin is expressed at high levels by all cones in the ventral mouse retina.[10] Thus, calcium-dependent changes in fluorescence can be measured in retinal interneurons or RGCs in ventral mouse retina while stimulating the cone photoreceptors with near-ultraviolet light. The mouse has become a major model of visual processing because of its tractable genetics, making this system well suited to a wide variety of retinal studies.[11]

We demonstrate and validate the utility of the system in two ways. First, we used mice that express Cre recombinase under the control of parvalbumin promoter (PVCre) to express GCaMP6f in a subset of RGCs. We presented a battery of visual stimuli including a full-field amplitude- and frequency-modulated stimulus (a.k.a. "chirp" stimulus),[1] moving bars, checkerboard noise, full-field light steps, and local bright/dark spots while imaging calcium-dependent changes in fluorescence. We were able to functionally classify the GCaMP6f-expressing RGCs into eight distinct types, consistent with anatomical studies of PV-expressing RGCs.[12,13] Second, we used mice that express Cre recombinase under the control of the PCP2 promoter (PCP2Cre) to express GCaMP6f in a subset of bipolar cells (BCs). We were able to resolve hundreds of individual synaptic release sites in BC axon terminals, measure calcium responses to visual stimuli, and functionally classify BCs into distinct ON and OFF types.[14,15] These results demonstrate that 1-photon light-sheet imaging is a relatively affordable and viable platform for monitoring and functionally characterizing neural activity across large populations of retinal neurons with high spatial resolutions.

RESULTS

1-photon light-sheet microscope for stimulus delivery and retinal imaging

The microscope system features three main units: (1) a light-sheet fluorescence excitation system, (2) a fluorescence emission detection system, and (3) a visual stimulus delivery system (Figure 1A). The collimated beam from the laser is transformed by a set of relay lenses and a cylindrical lens to generate a Gaussian light sheet that is focused by the illumination objective at the position of the sample. The lateral and longitudinal extent of the light sheet is controlled by a set of apertures. The thickness of the light sheet is controlled by a horizontal slit and the numerical aperture of the illumination objective. The center of the excitation plane is aligned with the detection axis by adjusting the position of the illumination objective (Figure 1A).

For imaging, the dissected retina was placed inside a chamber with RGC side facing down

The excitation light sheet was directed parallel to the plane of the retina containing the GCaMP-expressing cells. Images were acquired at 10–50 Hz, with a field of view of 700–1500 μm along

each dimension. Spatial binning was used to improve the signal-to-noise ratio of the acquired images. An operating laser diode power of 0.1–15 mW, corresponding to 0.01–1.5 mW power at the sample, was found to be adequate for detecting spontaneous and stimulus evoked activity in RGCs.

The visual stimulus for targeting photoreceptors was displayed by a digital light projector (DLP) with a 385 nm LED. The stimulus was delivered to the retina through the objective used for imaging fluorescent emission. To focus the stimulus on the photoreceptor plane without changing the plane of imaging, the position of the DLP relative to the microscope tube lens was adjusted (Figure 1A; see also STAR Methods). This allowed moving the visual stimulus focal plane by ~250 μm, sufficient to span the entire thickness of the mouse retina[16] (Figure 1B).

Axial spread of light sheet from scattering

A key aspect that controls the quality of images of biological tissues is scattering. The more the excitation light is scattered, the higher the background illumination and the worse the image quality. In 1-photon light-sheet imaging, scattering of excitation light can increase the effective thickness of the light sheet and thus reduce the resolution and image contrast.[17]

To determine the impact of scattering on the thickness of the light sheet, we first measured the effective thickness. This was achieved by imaging 500 nm fluorescent beads embedded in agarose[18] (Figure 1C). Agarose has a scattering coefficient of ~1 cm^{-1}[19] and therefore minimally scatters light. The depth of field estimated by fitting the measured axial intensity profile of individual beads with a Gaussian function was 8.5 ± 2.8 μm (Figure 1D). Next, we modeled the Airy disk profile as a Gaussian with standard deviation equal to the theoretical depth of field and then deconvolved it from the measured intensity profile to obtain the true thickness of the light sheet. With a theoretical depth of field 3.48 μm (Equation 5 in STAR Methods), the true thickness of the light sheet was 7.75 μm.

The retina has a scattering coefficient of 56.8 cm^{-1},[20] meaning that it scatters 1-photon excitation light more than agarose. To determine the effective thickness of the 488 nm light sheet in the retina, we imaged individual axon varicosities of RGCs (Figure 1E). The varicosities are ~1–4 μm[21] and exhibit robust calcium fluorescence from action potential-induced calcium influx,[22] thus acting as proxies for fluorescent beads. With a measured depth of field ~22.2 ± 8.1 μm, averaged over n = 26 varicosities (Figure 1F), and using the above deconvolution procedure, the effective thickness of the light sheet was obtained as 21.72 μm. This indicates that the light sheet, when directed at the ganglion cell layer and/or the IPL, remains well confined to these laminae[16] and does not strongly intersect with the photoreceptor layer.

Targeting S-cones for visual stimulation

A challenge with fluorescence imaging in the retina is that photoreceptors are exquisitely light sensitive and therefore can be activated by even a small amount of scattered light. The excitation will depend on the overlap between the opsin action spectrum and the excitation wavelength. To overcome this challenge, we targeted our experiments to the ventral mouse retina because the cones in this region predominantly express a S-opsin that is maximally sensitive to 360 nm (Figures 2B and 2C).[10,23] Light sensitivity of this S-opsin at the fluorescent excitation wavelength of 488 nm is ~4 orders of magnitude lower than its peak sensitivity. This further reduced the effect of light-sheet scatter on cone photoreceptor excitation. Calibration experiments indicated that the rate of S-opsin activation from the scattered 488 nm excitation light was ~10 photoisomerizations (P*)/S-cone/s (Figure S1; see also STAR Methods). By comparison, the intensity of the visual stimulus delivered at 385 nm near the peak S-opsin sensitivity[10,23] produced ~10^5 P*/S-cone/s. Thus, the scattered light was ~0.01% of the mean visual stimulus, below the contrast detection sensitivity of cones.[24]

Calcium fluorescence signals in active RGCs

To image calcium activity in RGCs, we used ventral retinas from Ai148; PVCre mice (Figure 2B).[25,26] Robust GCaMP6f fluorescence was observed in the somata, axons, and dendrites of RGCs (Figures 2D–2G). The density of somatic labeling averaged across four non-overlapping regions over the field of view was 1,081.04 ± 230.23 mm^{-2}. To extract and analyze the changes in calcium-dependent fluorescence resulting from visual stimulation of the photoreceptors, fluorescence images were first denoised, corrected for non-uniform illumination, and then processed using a semi-automated algorithm[27] (see STAR Methods; Figure 2D). Specifically, a threshold signal-to-noise ratio[27] of 8 and a pixel intensity correlation of 0.8 were used to detect and process the signals from fluorescent somata. In a typical experiment, this yielded several hundred active RGCs in the field of view (Figure 3A). We were also able to measure spontaneous and stimulus-driven calcium responses from primary and secondary dendrites of individual RGCs (Figure 2G). These data confirmed the system's capability for imaging large-scale neural activity in the retina.

Response classification of RGCs using full-field chirp and checkerboard noise stimuli

To validate the quality of fluorescence measurements from RGC somata, we tested the reliability of functionally classifying RGCs based on the changes in fluorescence produced by visual stimuli. Previous studies show that PV is expressed in 8 morphologically distinct RGC types,[12,13] suggesting an equivalent number of functionally distinct RGC types expressing GCAMP6f in the Ai148; PVCre mice. To classify the RGCs, we presented a chirp visual stimulus[1] (Figure 3B). This stimulus consists of a full-field light step, followed by full-field frequency- and amplitude-modulated sinusoidal illumination. Calcium-dependent fluorescence changes in 375 RGCs (n = 1 retina) were acquired over a field of view ~2.25 mm^2 (Figures 3A and 3B). Singular value decomposition (SVD) was applied to the temporal fluorescence traces, and leading principal components were used to generate a projection hyperspace (Figure 3C, left; also see STAR Methods). Fitting a Gaussian mixture model to the projection space yielded 8 clusters (Figure 3C, right). The discriminability of the clusters was assessed by comparing the inter-cluster Euclidean distance with the intra-cluster Euclidean distance (Figure 3D). Accuracy of clustering was determined by cross-validating clusters from alternative clustering methods such as hierarchical agglomerative clustering (HAC)[28] and spectral clustering (SC).[29] Each clustering algorithm produced identical results (Figure S2).

Based on the temporal response properties to different phases of the chirp stimulus, each cluster of RGCs was further

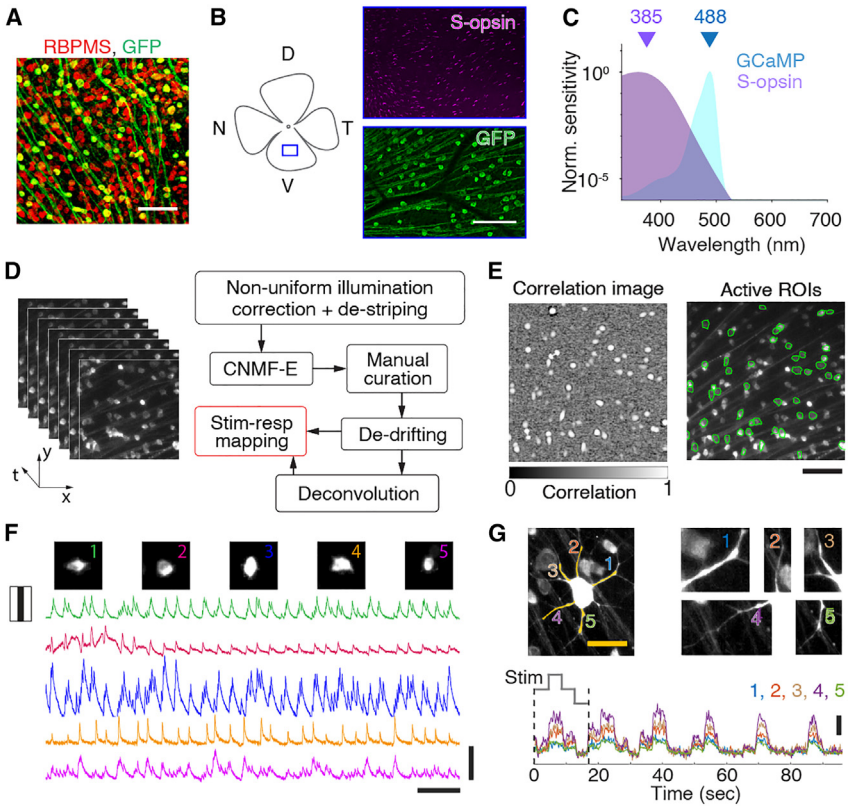

Figure 2. Imaging calcium responses of RGCs

(A) RGCs in retina from Ai148; PVCre mouse immunolabeled with pan-RGC marker RBPMS (red) and with GFP (green: GCaMP6f). Scale bar: 50 μm.

(B) Left: ventral retina used for fluorescence imaging. Right: immunolabeling for S-opsin in cone photoreceptors (magenta) and GFP (green: GCaMP6f). Scale bar: 100 μm.

(C) Visual stimuli delivered at 385 nm (purple arrow) near the peak spectral sensitivity of S-opsin (purple shaded area). Laser excitation at 488 nm (blue arrow) matched to the peak excitation of GCaMP (blue shaded area).

(D) Image analysis pipeline for extracting spontaneous or visual stimulus-evoked calcium responses and inferred spikes of RGCs. CNMF-E, constrained non-negative matrix factorization for micro-endoscopic data.

(E) Left: spatiotemporal response correlation image. Gray bar: correlation coefficient. Right: outlines (green contours) of active RGCs. Scale bar: 100 μm.

(F) Fluorescent images of representative RGC somata (top) and their temporal responses (bottom) to moving bars. Vertical scale bar: 20 (units of SNR, 6 dB cutoff). Horizontal scale bar: 200 s.

(G) Calcium activity in dendrites of a representative RGC to repeated full-field light steps (gray trace, bottom). Horizontal scale bar: 20 μm. Dashed vertical lines indicate duration of a single trial; total n = 6 trials. Temporal traces for 5 dendrites (top right) are shown in color. Vertical scale bar: 2 (units of SNR, 6 dB cutoff).

assigned to distinct functional types: ON, OFF, ON-OFF, transient, and sustained (Figures 3E and 3F). The RGCs in each cluster also exhibited a mosaic-like regularity in their spatial arrangement,[30] with nearest-neighbor spacing ranging from 70 to 120 μm for different types and a conformity ratio[31] between 1 and 3.4 (Figures 3G and 3H). This suggests that each cluster represents a functionally distinct RGC type.[32–34]

To examine the contrast polarity and temporal integration properties of RGCs, we characterized the spatiotemporal receptive fields (RFs) of RGCs from their changes in fluorescence during the presentation of checkerboard noise. Spike trains were estimated from calcium signals, and calcium transients associated with at least 1 spike were used to estimate the RF (see STAR Methods; Figure 3I). RGCs classified as ON brisk transient and OFF brisk transient types from responses to the chirp stimulus exhibited ON- and OFF-center responses, respectively (Figure 3J). The temporal responses exhibited positive and negative contrast preferences immediately preceding putative spikes (estimated from the calcium signals), with a biphasic profile consistent with previous findings for these RGC types.[30,35]

Direction- and orientation-selective responses of RGCs

To identify direction-selective (DS) RGCs, we imaged calcium responses of RGCs to bright bars (100% contrast) moving along 12 different directions. We calculated a direction-selective index (DSI) using the area under the temporal fluorescence trace for different movement directions (see STAR Methods). RGCs with a DSI greater than 0.3 were classified as DS-RGCs[36,37] (Figures 4A, 4B, and 4D). Prolonged exposure to excitation light can bleach GCaMP, thereby reducing its sensitivity over time.[6] This can bias DSI estimates obtained from trial-averaged responses. Therefore, only trial blocks in which the DSI did not change by more than 20% of that estimated from the first trial were included in the analysis (50% of trials, n = 6 trials). A total of 29 RGCs were identified as direction selective (Figure 4D), out of which 21 had clear ON and OFF responses (Figure 4B, inset). The ON-OFF DS-RGCs were further classified into 4 subtypes[38] based on orthogonality of preferred directions (Figure 4E). A similar fraction of DS-RGCs (~10%) were estimated from retinas of other Ai148; PVCre mice (n = 4).

To identify orientation-selective (OS) RGCs, we measured calcium responses to drifting gratings presented at different orientations (Figure 4C). Orientation selectivity was quantified by an orientation-selective index (OSI) (see STAR Methods). To distinguish OS-RGCs from DS-RGCs, we calculated the DSI of OS-RGCs from their responses to moving bars. A total of 31 RGCs that had OSI >0.3 and DSI <0.3 were classified as OS (Figure 4F). Note, it is possible some of these RGCs are bidirection selective and not OS per se. However, OS cells have been described previously in the retina,[39] while bidirection-selective cells have not.

Calcium imaging at BC axon terminals

Finally, we tested whether the system's resolution allows for imaging calcium activity at synaptic release sites. For this, we used retinas from Ai148; PCP2Cre transgenic mice that express GCaMP6f primarily in rod BCs but also exhibit some Cre

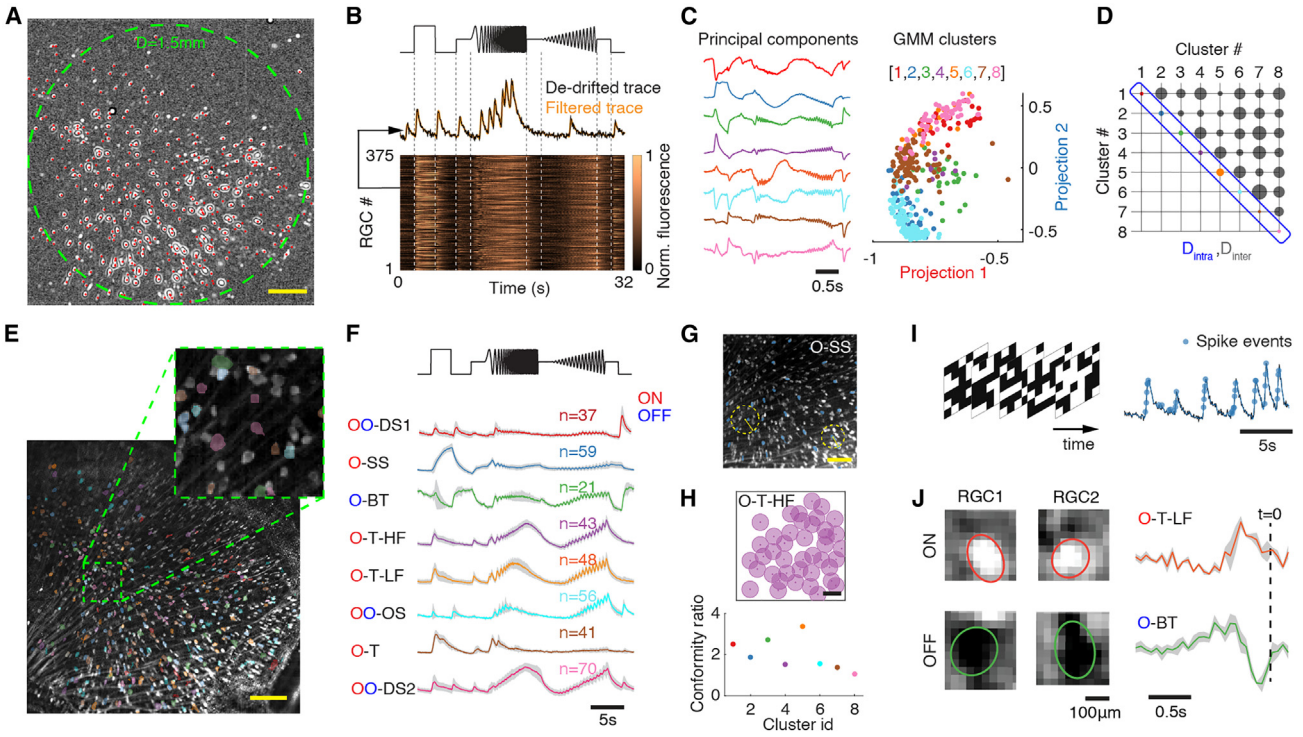

Figure 3. Classification of RGCs from population calcium responses

(A) Response correlation image over imaging field of view. Red filled circles: active RGCs, n = 375. Green dashed circle: 1.5 mm diameter. Scale bar: 200 μm.

(B) Top: chirp stimulus trace (black). Middle: baseline corrected (black) and filtered (orange) temporal response of a representative RGC. Bottom: heatmap of temporal fluorescent traces of n = 375 RGCs.

(C) Left: 8 leading principal components of the normalized temporal responses in (B). Right: Gaussian mixture model (GMM) fit to projection values in 8D hyperspace shown in a 2D plane. Clustered projection values (n = 8 clusters) are shown by colored circles.

(D) Mean pairwise Euclidean distance between projection values within each cluster (D_{intra}) and between clusters (D_{inter}) are illustrated by circles along the diagonal and the off-diagonal, respectively. The radius of each circle represents the Euclidean distance. Color scheme for diagonal elements same as in (C).

(E) Median intensity projection image with overlaid patches showing soma locations of active RGCs. Patch color corresponds to the clusters in (C). Scale bar: 200 μm. Inset: magnified view of an image patch.

(F) Mean temporal responses (colored solid line) of RGCs from different clusters to the chirp stimulus (black trace, top). ON, O (red); OFF, O (blue); DS, direction selective; SS, slow sustained; BT, brisk transient; T-HF, transient high frequency; T-LF, transient low frequency; OS, orientation selective; T, transient. Shaded error bar: SEM.

(G) Image showing RGC locations (blue patches) from representative group 2. Dashed circle and box (yellow) depict nearest-neighbor RGCs. Scale bar: 100 μm.

(H) Top: representative mosaic of O-T-HF RGCs. Radius of circle: mean nearest-neighbor distance (NND). Bottom: NND conformity ratio for different clusters in (F) indicated by the color of circles.

(I) Checkerboard pattern stimulus (checker size ~40 μm), corresponding response trace of a representative RGC (black), and inferred spikes (light blue circles).

(J) Spatial RFs of representative RGCs (left) and mean temporal RFs across all cells (right, solid line) belonging to ON transient low frequency and OFF brisk transient types. Time of spike: t = 0. Shaded error bar: SEM.

expression in type 2 and type 6 BCs.[14,15,40] Depolarization of BCs causes calcium influx at the axon terminal release sites, prior to glutamate release,[22] making these release sites ideal for calcium imaging. Light-sheet excitation was first targeted to the inner portion of the IPL adjacent to the ganglion cell layer, where the majority of release sites were observed. Fluorescence was observed in clusters of puncta (~1–4 μm diameter) across the imaging field, consistent with the size and density of release sites at BC terminals (Figures 5A and 5B).

In the absence of visual stimuli, the fluorescence was relatively weak across the different release sites (Figure 5B). To visually stimulate the BCs (via the photoreceptors), bright and dark spots were presented at different locations (Figure 5C; see also STAR Methods). A bright spot on a dark background induced strong fluorescence transients across hundreds of release sites within a 730 × 730 μm field of view (Figure 5B, left). Following disappearance of the spot, the fluorescence rapidly decayed to baseline (time constant of decay: 1.03 s), indicating that these responses are produced by calcium influx at the axon terminals of ON BCs (likely a combination of both rod BCs and types 6 cone BCs) (Figures 5E and 5F).

By contrast, a fraction of the release sites exhibited a transient increase in fluorescence following a dark spot on a bright background, but these sites were sparser, and their response amplitudes were smaller compared with the release sites that responded to bright spots on a dark background. We hypothesized that we were imaging calcium influx associated with glutamate release from OFF BCs (likely type 2 BCs). To image these

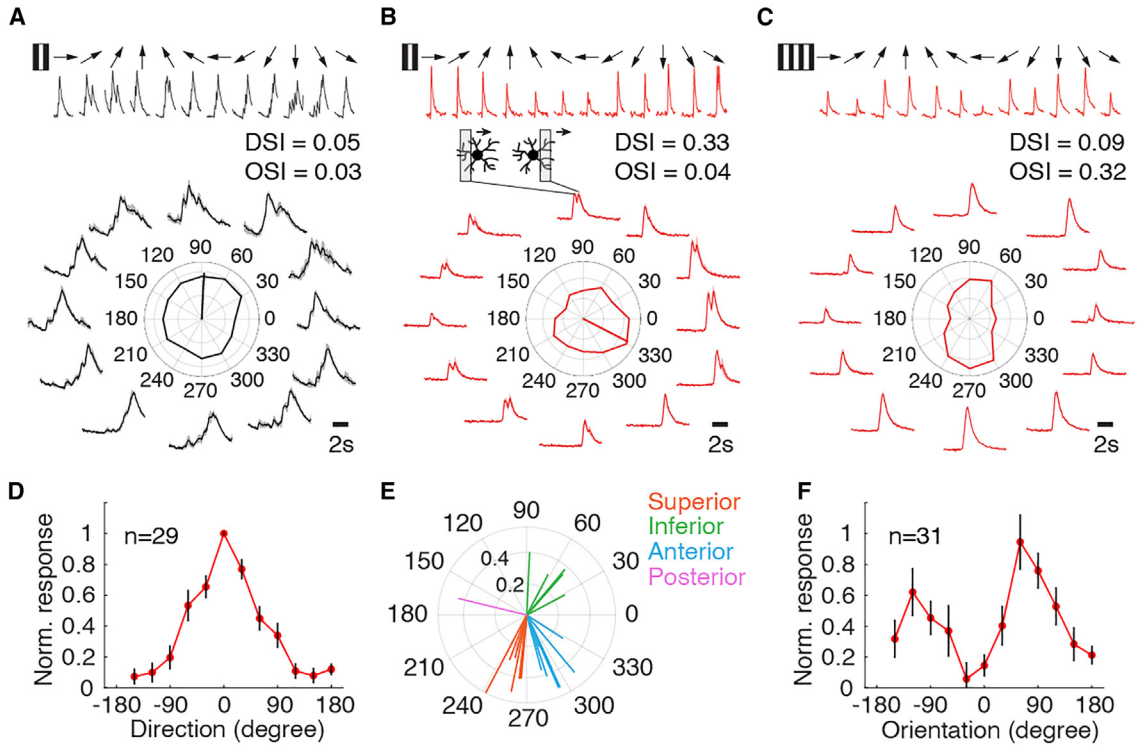

Figure 4. DS and OS responses of RGCs

(A) Response of a non-DS RGC. Top: a bright bar moving on a dark background along 12 directions. Bottom: trial-averaged calcium responses to different directions of bar movement. Gray shaded error bar is SD. The polar plot in the center shows normalized response and preferred direction of the RGC. DSI, direction-selective index; OSI, orientation-selective index.

(B) Same as in (A) but for an ON-OFF DS-RGC. Inset illustrates ON and OFF responses elicited by a bright bar entering and exiting the receptive field of the RGC.

(C) Same as in (A) but for an OS-RGC.

(D) Mean tuning curve of DS-RGC population (n = 29 RGCs from one retina). Black error bar is SD.

(E) Preferred directions of ON-OFF DS-RGC subtypes (n = 21 RGCs from one retina).

(F) Mean tuning curve of OS-RGC population (n = 31 RGCs from the same retina as in Figure 3). Black error bar is SD.

responses, the plane of excitation light sheet and the focal plane of the objective were moved toward the outer portion of the IPL by ~10 μm, which is dominated by the axon terminals of OFF BCs. However, this had a minor impact on the clarity of the signals. This is probably because the fluorescence activity of the OFF BC terminals was masked by the background fluorescence of the ON BC axon terminals. To unmask these OFF responses, we blocked the ON pathway using L-AP4—an mGluR6 agonist.[41] Blocking the fluorescence activity of the ON BCs significantly improved the signal-to-noise ratio (SNR) of the imaged OFF responses, allowing unambiguous identification of these release sites (Figures 5D–5F). The responses rose and decayed sharply to the appearance and disappearance of the dark spot (Figures 5D and 5E), with temporal characteristics distinct from ON BCs (time constant of decay: 0.82 s), indicating that these responses were from OFF BCs.

Finally, we sought histological identification of the BCs whose terminal responses were measured. We used antibodies against NK3R, which label type 1 and 2 BC types, and against Syt2, which label type 2 and 6 BC types.[42] Antibodies against GFP were used to amplify the expression of GCAMP6f. Release sites in the OFF sublayer that were labeled by GFP were also labeled by NK3R and Syt2, indicating that these sites were from type 2 BCs (Figure S3). Multiple terminal sites in the OFF sublayer were labeled only by NK3R, indicating they were from type 1 BCs.[42] These sites did not co-label with GFP, so they did not contaminate the imaging experiments. In the ON sublayer, a subset of the release sites was co-labeled by GFP and Syt2, indicating they were from type 6 BCs. The other fraction was co-labeled by GFP and PKCα, indicating they were from rod BCs[43] (Figure S3). This confirmed that ON calcium responses were from release sites of type 6 BCs and rod BCs (Figures 5D and 5E) and that OFF calcium responses were from release sites of type 2 BCs, respectively.

DISCUSSION

We present a 1-photon light-sheet imaging system that allows for measurements of neural activity across large populations of retinal neurons at synaptic resolution while simultaneously presenting visual stimuli to photoreceptors. The widefield planar sheet of light is confined to a layer ~20 μm thick, which allows for imaging activity in large cohorts of neurons confined to specific layers in the retina via calcium-dependent changes in fluorescence. An axial

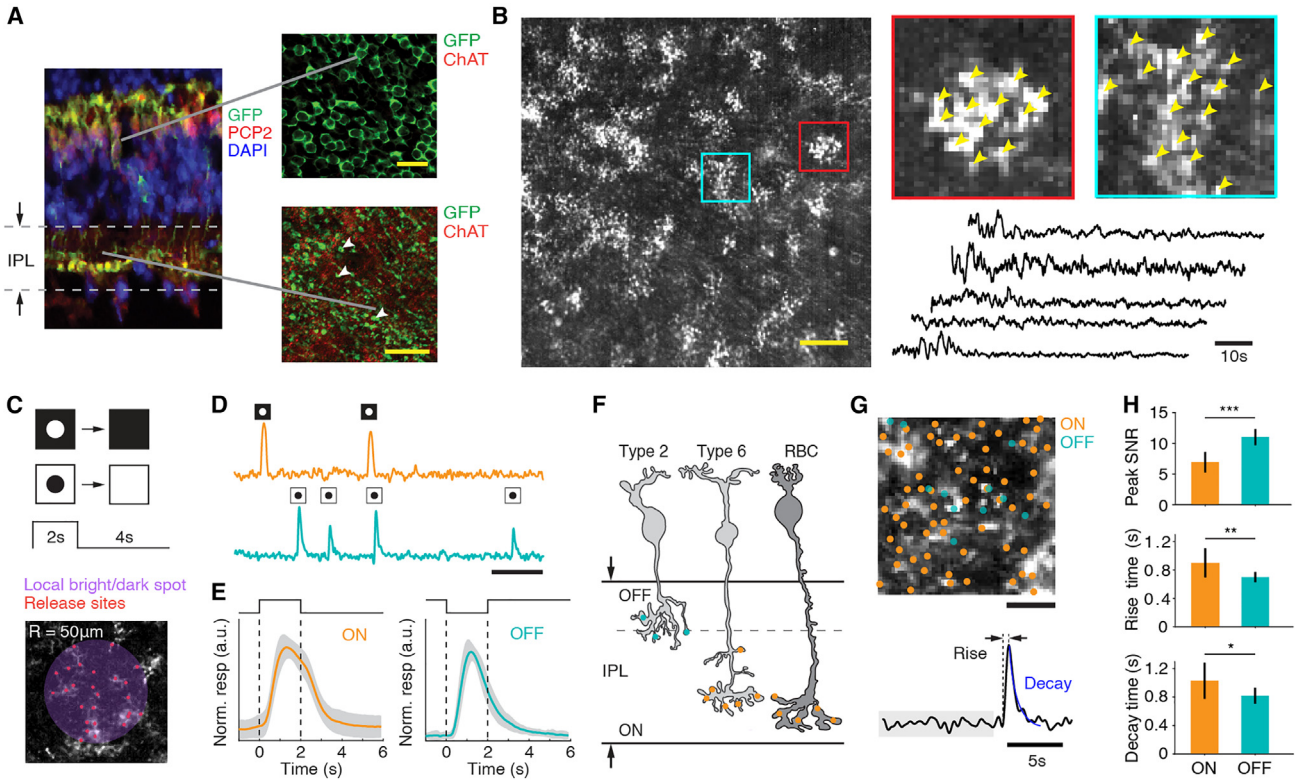

Figure 5. Calcium imaging of BC axon terminals

(A) Left: co-localization of GFP (green) and PCP2 (red) showing soma and terminals of BCs in the retina of an Ai148; PCP2Cre mouse. DAPI: blue. Right: flat-mount view of somata (top) and axon terminals (bottom). Scale bar: 20 μm.

(B) Left: SD projection image showing active release sites. Scale bar: 100 μm. Right: magnified view of regions indicated in red and cyan with spatial footprints (yellow arrows). Spontaneous responses (black traces) of 5 randomly selected release sites.

(C) Top: 100 μm diameter spots at 100% positive and negative contrasts are presented for 2 s at n = 34 locations. Bottom: representative spot (shaded circle) and active sites (red dots).

(D) Representative temporal fluorescent responses of a release site stimulated by a bright spot (top, orange), and a dark spot with 50 μM L-AP4 (bottom, teal), appearing at these locations at random times (n = 5 repeats for each location). Scale bar: 20 s.

(E) Normalized calcium transients to bright (left) and dark (right) spots, respectively, averaged over n = 504 (ON, orange) and n = 156 (OFF, teal) release sites. Dashed vertical lines indicate duration of the spot. Solid curve: mean. Shaded error bar: SD.

(F) Schematized structure of a type 2, a type 6, and a rod BC and their axonal arbors in the inner plexiform layer (IPL). Orange and teal filled circles represent putative release sites in the OFF and the ON layers, respectively.

(G) Top: release site locations on the SD projection image. Scale bar: 20 μm. Bottom: representative trace (black) of calcium transient used for estimating rise time, baseline fluctuations (gray), and time of decay (blue).

(H) Ratio of peak value of calcium transient to the SD of baseline response (top), rise time (middle), and decay time constant from exponential fit (bottom) for ON (n = 504, orange) and OFF (n = 156, teal) release sites. Mean, SD, and p values with Bonferroni correction are 6.92 ± 1.72 (ON), 13.15 ± 1.52 (OFF), $p = 3.9 \times 10^{-7}$ (top); 0.93 ± 0.22 (ON), 0.71 ± 0.10(OFF), 5.21×10^{-3} (middle); and 1.03 ± 0.25 (ON), 0.82 ± 0.11 (OFF), 3.1×10^{-2} (bottom).

All OFF responses in (D), (E), (G), and (H) were obtained with L-AP4.

separation is maintained between the excitation plane for fluorescence imaging and the focal plane for visual stimulation of the photoreceptors. Using this system, we were able to measure spontaneous and visual stimulus-dependent responses of hundreds of RGCs routinely over a retinal area 1.5–2.25 mm^2, corresponding to 50°–80° of visual angle in the mouse retina (Figure 3A). The SNR of the measured activity was sufficient to functionally classify RGCs in Ai148; PVCre retinas into 8 distinct types, consistent with previous morphological classification.[12,13] The resolution of the system also allowed measurements of calcium activity in individual synaptic release sites at BC axon terminals from Ai148; PCP2Cre retinas.

Optical imaging techniques that allow monitoring ensemble activity of neurons within biological specimens can offer key insights into how sensory signals are processed within specialized neural circuits. For example, 2-photon calcium-dependent fluorescence imaging[1,4,38] has been widely used in both retinal and cortical research for several reasons: (1) it provides high spatial resolution; (2) infrared light scatters less than shorter-wavelength light, which facilitates imaging deep into the tissue; and (3) infrared light reduces the activation of photoreceptors when imaging retinal neurons. However, this approach requires a costly and complex pulsed femtosecond laser and provides data with either poor temporal resolution or limited scan areas due to point laser scanning.

Light-sheet fluorescence microscopy is an alternative imaging modality that utilizes planar illumination to optically section the sample, enabling rapid acquisition of images with high spatial resolution while minimizing photobleaching of the fluorescence indicator.[44] These advantages have led to an increased adoption of this technology for biomedical imaging, ranging from cultured tissues to *in vivo* imaging in small animals such as zebrafish and drosophila.[45] In particular, combining optical sectioning with synchronized delivery of excitation light[46] allows capturing of subcellular dynamics in living cells as well as 3D reconstruction of activity in living biological specimens.[47] However, constraints in delivering the planar excitation light orthogonal to the detection axis often require the sample to be embedded in agarose—a condition not ideal for *ex vivo* retina. This requires custom-designed systems that can accommodate the geometry of the sample for mounting and keep the sample viable for long-term imaging.

We found that light-sheet imaging allows robust measurements of calcium responses with high spatial resolution in *ex vivo* retina and therefore offers several benefits. First, confining the excitation light to a narrow plane limits scattering of excitation light in the retina and bleaching of GCaMP. Second, the ability to monitor neural activity at the resolution of single synapses across a large area will open the possibility of examining how excitatory and inhibitory synaptic inputs from genetically targeted interneurons are integrated over dendritic subcompartments. This can offer detailed insights into circuit-specific computations.[48] Third, measurements of activity simultaneously in multiple genetically targeted cell types, combined with pharmacological or optogenetic manipulations,[49] can help distinguish the role of different presynaptic cell types in shaping the gain and non-linearities of signal transfer. Fourth, measurements of large-scale neural activity in specific layers will enable characterization of how signal and noise correlations[50] impact the encoding and transmission of information about visual features by different populations of neurons. Our system also allows for multiplexing excitation light of different wavelengths that can be targeted to different retinal planes and for incorporating remote focusing and tunable lens[51] to perform rapid multiplane imaging in the retina. Given the versatility, flexibility, and high-throughput measurement capabilities of this light-sheet imaging platform, we envision this system becoming a useful tool for large-scale interrogation of functional connectivity between cell types in the retina.

Limitations of the study

A challenge in retinal fluorescence imaging using 1-photon light sheet is scattering of the excitation light. The 488 nm light scattered within the retina can potentially reach the photoreceptors and activate M-opsin in cones. Another challenge is contamination of fluorescence signals from neurites and other structures such as axon bundles expressing GCaMP (Figure 3E). Faster, brighter, and long-wavelength-sensitive indicators,[7,52] as well as soma- and dendrite-directed calcium indicators,[53] can help overcome these challenges. 2-photon light-sheet imaging with the use of infrared lasers[47] can also be incorporated into our framework to improve spatial resolution and move the wavelength of the excitation light further away from the wavelengths to which M-opsin and rhodopsin are sensitive. The use of PCP2Cre mice limited our ability to unambiguously classify the release sites into functionally distinct BC types (Figure 5E). Future studies using transgenic mouse lines targeting specific BC types, or viral vector-based targeting with promoters specific to BC types, could provide clarity on how release sites that belong to different BC types differ in their spatiotemporal response properties.

STAR★METHODS

Detailed methods are provided in the online version of this paper and include the following:

- KEY RESOURCES TABLE
- RESOURCE AVAILABILITY
  - Lead contact
  - Materials availability
  - Data and code availability
- EXPERIMENTAL MODEL AND SUBJECT DETAILS
  - Animals
- METHOD DETAILS
  - Retina preparation
  - Light sheet excitation
  - Visual stimulation and calcium imaging
  - Immunohistochemistry and confocal imaging
- QUANTIFICATION AND STATISTICAL ANALYSIS
  - Theoretical thickness of light-sheet
  - Axial resolution and depth of field
  - Scattering of excitation light
  - Depth of field of imaging
  - Active ROIs, calcium responses and inferred spikes
  - Response clustering and RGC classification
  - Optimality and accuracy of clustering
  - Quantification of stimulus preference
  - Receptive field estimation
  - BC response characterization
  - Statistical analysis

SUPPLEMENTAL INFORMATION

Supplemental information can be found online at https://doi.org/10.1016/j.crmeth.2023.100453.

ACKNOWLEDGMENTS

This work was supported by NIH Brain Initiative grant 1R34NS111645-01 (G.D.F.) and NIH K99EY032119 award (S.R.). We thank members of the Field lab for comments on the manuscript.

AUTHOR CONTRIBUTIONS

Conceptualization, S.R., A.S., and G.D.F.; design of microscope, S.R., D.W., and Y.G.; design and tests of the retina chamber, A.M.R.; calibration of imaging system, investigation, and image analysis, S.R.; data curation, S.R. and B.P.; mouse genetics and planning, M.T. and M.L.S.; visualization, S.R.; writing – original draft, S.R. and G.D.F.; writing – review & editing, S.R., A.S., Y.G., and G.D.F.

DECLARATION OF INTERESTS

The authors declare no competing interests.

CellPress
OPEN ACCESS

Received: December 2, 2022
Revised: March 5, 2023
Accepted: March 24, 2023
Published: April 24, 2023

REFERENCES

1. Baden, T., Berens, P., Franke, K., Román Rosón, M., Bethge, M., and Euler, T. (2016). The functional diversity of retinal ganglion cells in the mouse. Nature *529*, 345–350. https://doi.org/10.1038/nature16468.
2. Ota, K., Oisi, Y., Suzuki, T., Ikeda, M., Ito, Y., Ito, T., Uwamori, H., Kobayashi, K., Kobayashi, M., Odagawa, M., et al. (2021). Fast, cell-resolution, contiguous-wide two-photon imaging to reveal functional network architectures across multi-modal cortical areas. Neuron *109*, 1810–1824.e9. https://doi.org/10.1016/j.neuron.2021.03.032.
3. Svoboda, K., and Yasuda, R. (2006). Principles of two-photon excitation microscopy and its applications to neuroscience. Neuron *50*, 823–839. https://doi.org/10.1016/j.neuron.2006.05.019.
4. Denk, W., Strickler, J.H., and Webb, W.W. (1990). Two-photon laser scanning fluorescence microscopy. Science *248*, 73–76. https://doi.org/10.1126/science.2321027.
5. Poleg-Polsky, A., and Diamond, J.S. (2016). Retinal circuitry balances contrast tuning of excitation and inhibition to enable reliable computation of direction selectivity. J. Neurosci. *36*, 5861–5876. https://doi.org/10.1523/JNEUROSCI.4013-15.2016.
6. Akerboom, J., Chen, T.W., Wardill, T.J., Tian, L., Marvin, J.S., Mutlu, S., Calderón, N.C., Esposti, F., Borghuis, B.G., Sun, X.R., et al. (2012). Optimization of a GCaMP calcium indicator for neural activity imaging. J. Neurosci. *32*, 13819–13840. https://doi.org/10.1523/JNEUROSCI.2601-12.2012.
7. Dana, H., Sun, Y., Mohar, B., Hulse, B.K., Kerlin, A.M., Hasseman, J.P., Tsegaye, G., Tsang, A., Wong, A., Patel, R., et al. (2019). High-performance calcium sensors for imaging activity in neuronal populations and microcompartments. Nat. Methods *16*, 649–657. https://doi.org/10.1038/s41592-019-0435-6.
8. Masland, R.H. (2012). The neuronal organization of the retina. Neuron *76*, 266–280. https://doi.org/10.1016/j.neuron.2012.10.002.
9. Jacobs, G.H., Neitz, J., and Deegan, J.F., 2nd. (1991). Retinal receptors in rodents maximally sensitive to ultraviolet light. Nature *353*, 655–656. https://doi.org/10.1038/353655a0.
10. Nadal-Nicolás, F.M., Kunze, V.P., Ball, J.M., Peng, B.T., Krishnan, A., Zhou, G., Dong, L., and Li, W. (2020). True S-cones are concentrated in the ventral mouse retina and wired for color detection in the upper visual field. Elife *9*, e56840. https://doi.org/10.7554/eLife.56840.
11. Huberman, A.D., and Niell, C.M. (2011). What can mice tell us about how vision works? Trends Neurosci. *34*, 464–473. https://doi.org/10.1016/j.tins.2011.07.002.
12. Laboissonniere, L.A., Goetz, J.J., Martin, G.M., Bi, R., Lund, T.J.S., Ellson, L., Lynch, M.R., Mooney, B., Wickham, H., Liu, P., et al. (2019). Molecular signatures of retinal ganglion cells revealed through single cell profiling. Sci. Rep. *9*, 15778. https://doi.org/10.1038/s41598-019-52215-4.
13. Münch, T.A., da Silveira, R.A., Siegert, S., Viney, T.J., Awatramani, G.B., and Roska, B. (2009). Approach sensitivity in the retina processed by a multifunctional neural circuit. Nat. Neurosci. *12*, 1308–1316. https://doi.org/10.1038/nn.2389.
14. Liang, C.Q., Zhang, G., Zhang, L., Chen, S.Y., Wang, J.N., Zhang, T.T., Singer, J.H., and Ke, J.B. (2021). Calmodulin bidirectionally regulates evoked and spontaneous neurotransmitter release at retinal ribbon synapses. eNeuro *8*, ENEURO.0257-20.2020. https://doi.org/10.1523/ENEURO.0257-20.2020.
15. Zhang, G., Liu, J.B., Yuan, H.L., Chen, S.Y., Singer, J.H., and Ke, J.B. (2022). Multiple calcium channel types with unique expression patterns mediate retinal signaling at bipolar cell ribbon synapses. J. Neurosci. *42*, 6487–6505. https://doi.org/10.1523/JNEUROSCI.0183-22.2022.
16. Ferguson, L.R., Dominguez, J.M., 2nd, Balaiya, S., Grover, S., and Chalam, K.V. (2013). Retinal thickness normative data in wild-type mice using customized miniature SD-OCT. PLoS One *8*, e67265. https://doi.org/10.1371/journal.pone.0067265.
17. Remacha, E., Friedrich, L., Vermot, J., and Fahrbach, F.O. (2020). How to define and optimize axial resolution in light-sheet microscopy: a simulation-based approach. Biomed. Opt Express *11*, 8–26. https://doi.org/10.1364/BOE.11.000008.
18. Jvakaitis, and Wilson. (1998). The measurement of the amplitude point spread function of microscope objective lenses. J. Microsc. *189*, 8–11.
19. Jacques, S.L. (2013). Optical properties of biological tissues: a review. Phys. Med. Biol. *58*, R37–R61. https://doi.org/10.1088/0031-9155/58/11/R37.
20. Sardar, D.K., Yow, R.M., Tsin, A.T.C., and Sardar, R. (2005). Optical scattering, absorption, and polarization of healthy and neovascularized human retinal tissues. J. Biomed. Opt. *10*, 051501. https://doi.org/10.1117/1.2065867.
21. Calkins, D.J., Tsukamoto, Y., and Sterling, P. (1998). Microcircuitry and mosaic of a blue-yellow ganglion cell in the primate retina. J. Neurosci. *18*, 3373–3385.
22. Pan, Z.H., Hu, H.J., Perring, P., and Andrade, R. (2001). T-type Ca(2+) channels mediate neurotransmitter release in retinal bipolar cells. Neuron *32*, 89–98. https://doi.org/10.1016/s0896-6273(01)00454-8.
23. Lyubarsky, A.L., Falsini, B., Pennesi, M.E., Valentini, P., and Pugh, E.N., Jr. (1999). UV- and midwave-sensitive cone-driven retinal responses of the mouse: a possible phenotype for coexpression of cone photopigments. J. Neurosci. *19*, 442–455.
24. Naarendorp, F., Esdaille, T.M., Banden, S.M., Andrews-Labenski, J., Gross, O.P., and Pugh, E.N., Jr. (2010). Dark light, rod saturation, and the absolute and incremental sensitivity of mouse cone vision. J. Neurosci. *30*, 12495–12507. https://doi.org/10.1523/JNEUROSCI.2186-10.2010.
25. Jo, A., Xu, J., Deniz, S., Cherian, S., DeVries, S.H., and Zhu, Y. (2018). Intersectional strategies for targeting amacrine and ganglion cell types in the mouse retina. Front. Neural Circuits *12*, 66. https://doi.org/10.3389/fncir.2018.00066.
26. Kim, T.J., and Jeon, C.J. (2006). Morphological classification of parvalbumin-containing retinal ganglion cells in mouse: single-cell injection after immunocytochemistry. Invest. Ophthalmol. Vis. Sci. *47*, 2757–2764. https://doi.org/10.1167/iovs.05-1442.
27. Zhou, P., Resendez, S.L., Rodriguez-Romaguera, J., Jimenez, J.C., Neufeld, S.Q., Giovannucci, A., Friedrich, J., Pnevmatikakis, E.A., Stuber, G.D., Hen, R., et al. (2018). Efficient and accurate extraction of in vivo calcium signals from microendoscopic video data. Elife *7*, e28728. https://doi.org/10.7554/eLife.28728.
28. Rokach, L., and Maimon, O. (2005). Clustering methods. In Data Mining and Knowledge Discovery Handbook, O. Maimon and L. Rokach, eds. (Springer US), pp. 321–352. https://doi.org/10.1007/0-387-25465-x_15.
29. Jordan, M.I., and Weiss, Y. (2002). On Spectral Clustering: Analysis and an Algorithm (MIT Press), p. 849.
30. Roy, S., Jun, N.Y., Davis, E.L., Pearson, J., and Field, G.D. (2021). Intermosaic coordination of retinal receptive fields. Nature *592*, 409–413. https://doi.org/10.1038/s41586-021-03317-5.
31. Field, G.D., Sher, A., Gauthier, J.L., Greschner, M., Shlens, J., Litke, A.M., and Chichilnisky, E.J. (2007). Spatial properties and functional organization of small bistratified ganglion cells in primate retina. J. Neurosci. *27*, 13261–13272. https://doi.org/10.1523/JNEUROSCI.3437-07.2007.
32. Devries, S.H., and Baylor, D.A. (1997). Mosaic arrangement of ganglion cell receptive fields in rabbit retina. J. Neurophysiol. *78*, 2048–2060. https://doi.org/10.1152/jn.1997.78.4.2048.
33. Field, G.D., and Chichilnisky, E.J. (2007). Information processing in the primate retina: circuitry and coding. Annu. Rev. Neurosci. *30*, 1–30. https://doi.org/10.1146/annurev.neuro.30.051606.094252.

34. Wässle, H., Boycott, B.B., and Illing, R.B. (1981). Morphology and mosaic of on- and off-beta cells in the cat retina and some functional considerations. Proc. R. Soc. Lond. B Biol. Sci. *212*, 177–195. https://doi.org/10.1098/rspb.1981.0033.

35. Ravi, S., Ahn, D., Greschner, M., Chichilnisky, E.J., and Field, G.D. (2018). Pathway-specific asymmetries between ON and OFF visual signals. J. Neurosci. *38*, 9728–9740. https://doi.org/10.1523/JNEUROSCI.2008-18.2018.

36. Yao, X., Cafaro, J., McLaughlin, A.J., Postma, F.R., Paul, D.L., Awatramani, G., and Field, G.D. (2018). Gap junctions contribute to differential light adaptation across direction-selective retinal ganglion cells. Neuron *100*, 216–228.e6. https://doi.org/10.1016/j.neuron.2018.08.021.

37. Ray, T.A., Roy, S., Kozlowski, C., Wang, J., Cafaro, J., Hulbert, S.W., Wright, C.V., Field, G.D., and Kay, J.N. (2018). Formation of retinal direction-selective circuitry initiated by starburst amacrine cell homotypic contact. Elife *7*, e34241. https://doi.org/10.7554/eLife.34241.

38. Ding, H., Smith, R.G., Poleg-Polsky, A., Diamond, J.S., and Briggman, K.L. (2016). Species-specific wiring for direction selectivity in the mammalian retina. Nature *535*, 105–110. https://doi.org/10.1038/nature18609.

39. Chen, H., Liu, X., and Tian, N. (2014). Subtype-dependent postnatal development of direction- and orientation-selective retinal ganglion cells in mice. J. Neurophysiol. *112*, 2092–2101. https://doi.org/10.1152/jn.00320.2014.

40. Ivanova, E., Hwang, G.S., and Pan, Z.H. (2010). Characterization of transgenic mouse lines expressing Cre recombinase in the retina. Neuroscience *165*, 233–243. https://doi.org/10.1016/j.neuroscience.2009.10.021.

41. Thoreson, W.B., and Ulphani, J.S. (1995). Pharmacology of selective and non-selective metabotropic glutamate receptor agonists at L-AP4 receptors in retinal ON bipolar cells. Brain Res. *676*, 93–102. https://doi.org/10.1016/0006-8993(95)00093-6.

42. Wässle, H., Puller, C., Müller, F., and Haverkamp, S. (2009). Cone contacts, mosaics, and territories of bipolar cells in the mouse retina. J. Neurosci. *29*, 106–117. https://doi.org/10.1523/JNEUROSCI.4442-08.2009.

43. Negishi, K., Kato, S., and Teranishi, T. (1988). Dopamine cells and rod bipolar cells contain protein kinase C-like immunoreactivity in some vertebrate retinas. Neurosci. Lett. *94*, 247–252. https://doi.org/10.1016/0304-3940(88)90025-0.

44. Huisken, J., Swoger, J., Del Bene, F., Wittbrodt, J., and Stelzer, E.H.K. (2004). Optical sectioning deep inside live embryos by selective plane illumination microscopy. Science *305*, 1007–1009. https://doi.org/10.1126/science.1100035.

45. Keller, P.J., Schmidt, A.D., Santella, A., Khairy, K., Bao, Z., Wittbrodt, J., and Stelzer, E.H.K. (2010). Fast, high-contrast imaging of animal development with scanned light sheet-based structured-illumination microscopy. Nat. Methods *7*, 637–642. https://doi.org/10.1038/nmeth.1476.

46. Chen, B.C., Legant, W.R., Wang, K., Shao, L., Milkie, D.E., Davidson, M.W., Janetopoulos, C., Wu, X.S., Hammer, J.A., 3rd, Liu, Z., et al. (2014). Lattice light-sheet microscopy: imaging molecules to embryos at high spatiotemporal resolution. Science *346*, 1257998. https://doi.org/10.1126/science.1257998.

47. Truong, T.V., Supatto, W., Koos, D.S., Choi, J.M., and Fraser, S.E. (2011). Deep and fast live imaging with two-photon scanned light-sheet microscopy. Nat. Methods *8*, 757–760. https://doi.org/10.1038/nmeth.1652.

48. Diamond, J.S. (2017). Inhibitory interneurons in the retina: types, circuitry, and function. Annu. Rev. Vis. Sci. *3*, 1–24. https://doi.org/10.1146/annurev-vision-102016-061345.

49. Park, S.J.H., Pottackal, J., Ke, J.B., Jun, N.Y., Rahmani, P., Kim, I.J., Singer, J.H., and Demb, J.B. (2018). Convergence and divergence of CRH amacrine cells in mouse retinal circuitry. J. Neurosci. *38*, 3753–3766. https://doi.org/10.1523/JNEUROSCI.2518-17.2018.

50. Ruda, K., Zylberberg, J., and Field, G.D. (2020). Ignoring correlated activity causes a failure of retinal population codes. Nat. Commun. *11*, 4605. https://doi.org/10.1038/s41467-020-18436-2.

51. Fahrbach, F.O., Voigt, F.F., Schmid, B., Helmchen, F., and Huisken, J. (2013). Rapid 3D light-sheet microscopy with a tunable lens. Opt Express *21*, 21010–21026. https://doi.org/10.1364/OE.21.021010.

52. Qian, Y., Piatkevich, K.D., Mc Larney, B., Abdelfattah, A.S., Mehta, S., Murdock, M.H., Gottschalk, S., Molina, R.S., Zhang, W., Chen, Y., et al. (2019). A genetically encoded near-infrared fluorescent calcium ion indicator. Nat. Methods *16*, 171–174. https://doi.org/10.1038/s41592-018-0294-6.

53. Shemesh, O.A., Linghu, C., Piatkevich, K.D., Goodwin, D., Celiker, O.T., Gritton, H.J., Romano, M.F., Gao, R., Yu, C.C.J., Tseng, H.A., et al. (2020). Precision calcium imaging of dense neural populations via a cell-body-targeted calcium indicator. Neuron *107*, 470–486.e11. https://doi.org/10.1016/j.neuron.2020.05.029.

54. Doi, E., Gauthier, J.L., Field, G.D., Shlens, J., Sher, A., Greschner, M., Machado, T.A., Jepson, L.H., Mathieson, K., Gunning, D.E., et al. (2012). Efficient coding of spatial information in the primate retina. J. Neurosci. *32*, 16256–16264. https://doi.org/10.1523/JNEUROSCI.4036-12.2012.

55. Schindelin, J., Arganda-Carreras, I., Frise, E., Kaynig, V., Longair, M., Pietzsch, T., Preibisch, S., Rueden, C., Saalfeld, S., Schmid, B., et al. (2012). Fiji: an open-source platform for biological-image analysis. Nat. Methods *9*, 676–682. https://doi.org/10.1038/nmeth.2019.

56. Born, M., and Wolf, E. (2013). Principles of Optics: Electromagnetic Theory of Propagation, Interference and Diffraction of Light (Elsevier).

57. Baylor, D.A. (1987). Photoreceptor signals and vision. Proctor lecture. Invest. Ophthalmol. Vis. Sci. *28*, 34–49.

58. Govardovskii, V.I., Fyhrquist, N., Reuter, T., Kuzmin, D.G., and Donner, K. (2000). In search of the visual pigment template. Vis. Neurosci. *17*, 509–528. https://doi.org/10.1017/s0952523800174036.

59. Schwarz, G. (1978). Estimating the dimension of a model. Ann. Statist. *6*, 461–464.

STAR★METHODS

KEY RESOURCES TABLE

REAGENT or RESOURCE	SOURCE	IDENTIFIER
Antibodies		
anti-GFP	Rockland	Cat # 600-901-215; RRID: AB_1537402
anti-ChAT	Millipore Sigma	Cat # AB144P; RRID: AB_2079751
anti-PCP2	Santa Cruz Biotechnology, Inc.	Cat # sc-137064; RRID: AB_2158439
anti-NK3R	Dr. Arlene Hirano, Geffen School of Medicine at University of California, Los Angeles	N/A
anti-synaptotagmin II	Zebrafish International Resource Center, University of Oregon, Eugene, OR	Cat # ZDB-ATB-081002-25; RRID: AB_10013783
anti-PKCα	Novus Biologicals, LLC.	Cat # AF5340; RRID: AB_2168552
Alexa 405	Jackson ImmunoResearch Inc.	Cat # 705-475-003; RRID: AB_2340426
Alexa Fluor 488	Invitrogen	Cat # A-11094; RRID: AB_923386
Alexa Fluor 555	Invitrogen	Cat # A-31572; RRID: AB_162543
Alexa Fluor 647	Invitrogen	Cat # A-21447; RRID: AB_2535864
DAPI	Molecular Probes	Cat #S36964
Hoechst	Thermo Fisher Scientific	Cat #H3570
Experimental models: Organisms/strains		
Mus musculus (Ai148-D)	Jackson Laboratory	RRID: IMSR_JAX:030328
Mus musculus (PVCre)	Jackson Laboratory	RRID: IMSR_JAX:008069
Mus musculus (PCP2Cre)	Jackson Laboratory	RRID: IMSR_JAX:010356
Chemicals, peptides, and recombinant proteins		
Ames' media	Sigma Aldrich	Product # A1420
L-AP4	Tocris Bioscience	Cat # 0103
Phosphate buffered Saline	Santa Cruz Biotechnology, Inc.	Cat # sc-296028
Normal donkey serum	Jackson ImmunoResearch Labs, Inc.	Cat # 017-000-121
Bovine serum albumin	VWR	Cat # 97061-420
Triton X-100	Sigma Aldrich	Product # X-100
OCT media	VWR	Cat # 25608-930
Paraformaldehyde	VWR	Cat # IC0219998380
Deposited data		
Raw and analyzed data	This paper	https://doi.org/10.5281/zenodo.7747113
Software and algorithms		
MATLAB	The Mathworks, Inc., Natick, MA	R2021a (or later)
CAIMAN codebase	Zhou et al.[27]	N/A
Analysis scripts	This paper	https://doi.org/10.5281/zenodo.7747113
FIJI/ImageJ	National Institutes of Health	Version 1.53t (https://imagej.net/Fiji)
HC-Image Live	Hamamatsu; Boston, MA	N/A
NIS Elements	Nikon Instruments, Inc.	AR Version 4.5
Fusion 360	Autodesk, USA	Version 2.0.10811
Ultimaker Cura	Ultimaker, Utrech, Netherlands	Version 5.3

(*Continued on next page*)

Continued

REAGENT or RESOURCE	SOURCE	IDENTIFIER
Other		
Dialysis membrane	Spectra/Por RC	132677
500 nm diameter fluorescent polystyrene beads	Spherotech, Inc.	FICP-08-2
Continuous wave laser	Coherent, Inc.	OBIS 488LX
Collimator	Thorlabs, Inc.	F240APC-A
Relay lenses 1	Edmunds Optics, Inc.	47-365, 47-645
Cylindrical lens	Edmund Optics, Inc.	33–228
Excitation objective	Mitutoyo America Coorp.	MY5X-802
Relay lenses 2	Thorlabs, Inc.	LBF254-050
Slits	Thorlabs, Inc.	CP-20S, VA100C
Quartz cuvette	Thorlabs, Inc.	CV10Q35F
3D printer	Ultimaker	Ultimaker S3, S5
DLP	EKB Technologies, Ltd.	DPM-E4500LUVBGMKII
Aperture	Thorlabs, Inc.	SM1D12D
Aspheric converging lens	Thorlabs, Inc.	AL50100
Inverted Microscope	Nikon Instruments, Inc.	Ti-E
Imaging objective 10×	Nikon Instruments, Inc.	MRH00101
Imaging objective 20×	Nikon Instruments, Inc.	MRH08230
Photometer	Thorlabs, Inc.	PM100D
Imaging camera	Hamamatsu Photonics	ORCA Fusion Gen-III SCMOS
Dichroic mirror	Thorlabs, Inc.	DMLP425R
Edge filter	Semrock, Inc.	FF01-430/LP-25
GFP filter	Semrock, Inc.	GFP-3035D
DAQ device	National Instruments, Corp.	6550-USB
Cryostat	Leica, Inc.	CM3050
Laser scanning confocal microscope	Nikon Instruments, Inc.	Ti-2

RESOURCE AVAILABILITY

Lead contact

Further information and requests for resources and reagents should be directed to and will be fulfilled by the lead contact: Suva Roy (suva.roy@duke.edu).

Materials availability

This study did not generate new materials.

Data and code availability

- All data reported in this paper will be shared by the lead contact upon request.
- All original code used to analyze data is publicly available at https://doi.org/10.5281/zenodo.7747113.
- Further information for data and code to re-analyze data reported in this paper is available from the lead contact upon request.

EXPERIMENTAL MODEL AND SUBJECT DETAILS

Animals

Procedures for animal care and use followed guidelines approved by the Institutional Animal Care and Use Committee at Duke University. The Ai148 floxed mice carrying the GCaMP6f transgene under the control of tetracycline transactivator tTA2 (TIT2L-GC6f-ICL-tTA2) (Jackson Laboratory, 030328), were crossed to (1) PVCre mice carrying a Cre allele in parvalbumin (PV) expressing neurons (Jackson Laboratory, 008069), and (2) PCP2Cre mice carrying Cre allele in Purkinje cell protein (PCP2) expressing neurons (Jackson Laboratory, 010356), to obtain the Ai148; PVCre and Ai148; PCP2Cre mice respectively. Mice (n = 10 Ai148; PVCre and n = 6 Ai148; PCP2Cre) with age between 2 and 10 months of both sexes were used for experiments.

METHOD DETAILS

Retina preparation

Retinas for experiments were obtained following previously established protocols.[54] Briefly, mice were kept under 12 h light-dark cycle with *ad lib* access to food and water. For experiments, animals were dark-adapted for 12 h, then euthanized in complete darkness and under infrared illumination using infrared goggles. The eyes were enucleated, and retinas were dissected out in a petri dish containing sodium bicarbonate buffered Ames' media (Sigma Aldrich, A1420) bubbled with 95% oxygen and 5% carbon dioxide (pH 7.4, temperature maintained at 33°C). A piece of retina ~1.5 mm × 2 mm was cut from the ventral half and transferred to a custom-designed chamber containing oxygenated Ames' solution. The chamber has a glass bottom for imaging and a glass side window for entry of light-sheet excitation. The initial prototypes for the chamber were designed using Autodesk Fusion 360 and produced with Ultimaker S3 and S5. The retina was flattened gently using a hollow cylinder with a porous membrane (Spectra/Por RC dialysis membrane, 132677) that allows passage of solution and metabolites. The chamber containing the retina was transferred to the light-sheet microscope for imaging. Throughout the experiment, the retina was continuously superfused with oxygenated Ames' solution (described above) with a gravity-fed perfusion system.

Light sheet excitation

The excitation light was provided by a 488 nm laser (OBIS LX continuous wave laser, Coherent, Inc.). The laser beam was collimated using a fiber collimator (Thorlabs, Inc., F240APC-A) and expanded to 1 mm diameter by a pair of relay lenses with effective focal length 225 mm (Edmunds Optics, Inc., 47–365, 47–645). The expanded Gaussian beam is compressed by a cylindrical lens with focal length 50 mm (Edmund Optics, Inc., 33–228) and the resulting light-sheet is focused on the back aperture of the illumination objective (Mitutoyo, 5×, 0.14 NA, MY5X-802) by a pair of relay lenses of effective focal length 50 mm (Thorlabs, Inc., LBF254-050). A pair of orthogonal slits (Thorlabs, Inc., CP-20S, VA100C) controlled the lateral extent and the axial thickness of the light-sheet. The laser operating power was maintained between 0.1 and 15 mW, that produced 0.01–1.5 mW power at the sample. The depth of field was estimated by obtaining a stack of 200 images in 1 μm steps, of 500 nm diameter fluorescent polystyrene beads (Spherotech, Inc., FICP-08-2) embedded in agarose placed inside a quartz cuvette (Thorlabs, Inc., CV10Q35F).

Visual stimulation and calcium imaging

Visual stimuli were rendered using an OpenGL framework using custom written scripts in MATLAB (The Mathworks, Inc., Natick, MA). The stimulus patterns were streamed via an HDMI cable to the LightCrafter 4500 Digital Light Projector (DLP) (EKB Technologies, Ltd., DPM-E4500LUVBGMKII) and controlled by a custom GUI. The stimulus was displayed at 385 nm using a built-in LED, operated in the linear range. The display comprised of digital micromirrors arranged in a diamond pattern, with spatial resolution of 920 × 1040 pixels. To minimize spherical aberration of the projected stimulus image, a circular aperture (Thorlabs, Inc., SM1D12D) was placed in front of the DLP. The visual stimulus was collimated by a 100 mm aspheric converging lens (Thorlabs, Inc., AL50100) and the tube lens of Ti microscope (Nikon Instruments, Inc.). The final image was focused on the photoreceptors by a 10x Plan Fluor (Nikon Instruments Inc., MRH00101) or a 20x Super Plan Fluor (Nikon Instruments Inc., MRH08230) objective, rated to operate in the UV wavelength range, through the bottom glass surface of the chamber. The stimulus plane was offset from the imaging plane by controlling the distance between the DLP and the focusing lens (Figure 1A). This offset allowed us to simultaneously use the same objective for visual stimulus delivery, and imaging calcium dependent fluorescence in RGCs and BCs. The following set of stimuli were used in our experiments: (1) bright bar (100% Michelson contrast) traveling along 12 different directions with a speed of 480 m/s, (2) grating (100% Michelson contrast) moving along 12 different directions with a speed ranging between 24 and 100 m/s, (3) full-field 'chirp' sequence comprising of dark (3 s), bright (3 s), contrast frequency modulation (0.5–8 Hz, 8 s period) and contrast amplitude modulation (0.5–2 Hz, 8 s period), repeated 7 times, (4) full-field light increment and decrements, (5) binary checkerboard patterns with checker size 10–50 μm, and (6) local bright/dark spots (100 μm diameter) repeated 5 times at each location manually selected from a template image. L-AP4 (L-(+)-2-Amino-4-phosphonobutyric acid, Tocris Bioscience, 0103) at 50 μM was used to block mGluR6 receptors. The stimulus frames refreshed at 60 Hz. The stimulus brightness was calibrated using a photometer (Thorlabs, Inc., PM100D) and was set to ~10^5 P*/S-cone/s for experiments using neutral density filters (Thorlabs, Inc.).

Calcium images were captured by an ORCA Fusion camera (Hamamatsu Photonics) using the HC-Image software (Hamamatsu Photonics). GCaMP6f expression in RGC somas and BC terminals was reliably observed over a laminar depth of 20–30 μm. A long-pass dichroic mirror (Thorlabs, Inc., DMLP425R) was used to reflect the UV stimulus and transmit the GCaMP6f emission. A long-wave-pass edge filter (Semrock, FF01-430/LP-25) and a GFP filter (Semrock, GFP-3035D) were placed after the dichroic to block UV light and allow emitted light, respectively, to reach the camera. Images are acquired at 10–50 Hz, at 16-bit resolution, with spatial binning of 2 or 4. Pixel size of projected image was calibrated for each imaging objective using a glass reticle with 10 μm resolution. Calcium images were registered with visual stimuli by using timestamps from the camera and stored in the stimulus computer via a 6550-USB DAQ device (National Instruments, Corp.).

Immunohistochemistry and confocal imaging

Wholemount staining was performed on the retinas of Ai148; PVCre and Ai148; PCP2Cre mice. The retinas were fixed in 4% PFA for 45 min at room temperature and then incubated in 5% normal donkey serum (Jackson ImmunoResearch Laboratories Inc.,

017-000-121) in 1X phosphate buffer saline (PBS) with azide (Santa Cruz Biotechnology, SC-296028) containing 0.5% Triton X-100 (Sigma Aldrich, 93443), overnight at 4°C. The retinas were then incubated in primary antibodies on a rocker for 3–5 days at 4°C, after which they were rinsed in 1X PBS and incubated in secondary antibodies overnight at 4°C on a rocker. The retinas were then rinsed in 1X PBS, placed on a filter paper, and mounted on a glass slide with sealed coverslips. For cryosections, after fixation the retinas were incubated in 30% sucrose/PBS for 4–5 h, embedded in OCT (VWR, 25608-930), frozen using 95% ethanol in dry ice, and then sectioned at 15–20 μm thickness using a cryostat (Leica, CM3050). Sections were incubated sequentially with 0.5% Triton X-100, 1% bovine serum albumin (VWR, 97061-420), each for 1 h, then with primary antibodies overnight at 4°C, and with secondary antibodies for 1 h at room temperature. The mounted retinas were imaged with a laser scanning confocal microscope (Nikon Instruments, Inc., Ti-2) using 20x/40x/60× air objective. The z-stack of images were acquired using NIS Elements software, stored as .nd2 files and were further analyzed offline in FIJI software,[55] to identify laminae and GCaMP expressing cells.

The following primary antibodies were used: anti-GFP (1:1000, Rockland, 600-901-215), anti-ChAT (1:500, Millipore Sigma, AB144P), anti-PCP2 (1:500, Santa Cruz Biotechnology, Inc. sc-137064), anti-NK3R (1:750, generous gift from Arlene Hirano, Geffen School of Medicine at University of California, Los Angeles), anti-synaptotagmin II (Syt2, 1:200, Zebrafish International Resource Center, University of Oregon, Eugene, OR), and anti-PKCα (1:1000, Novus Biologicals, LLC., AF5340). Secondary antibodies conjugated to Alexa 405 (1:500; Jackson ImmunoResearch Inc., Code 705-475-003), Alexa 488 (1:500; Invitrogen, A-11094), Alexa 555 (1:500; Invitrogen, A-31572), and Alexa 647 (1:500; Invitrogen, A-21447), were each diluted at 1:500. DAPI (Molecular Probes, S36964) and Hoechst diluted in PBS (1:500, Thermo Fisher Scientific, H3570) was used for nuclear staining.

QUANTIFICATION AND STATISTICAL ANALYSIS

Theoretical thickness of light-sheet

The thickness of the light-sheet determines the axial range over which the sample can be reliably imaged. The light-sheet produced by the excitation optics (Figure 1A) has a Gaussian profile with a beam waist:

$$w = \frac{2\lambda_{exc}}{\pi\, NA} \quad \text{(Equation 1)}$$

Here, λ_{exc} is the wavelength of excitation light and NA is the numerical aperture of the illumination objective. If θ is the half angle of the light cone generated by the objective and n is the refractive index of the medium between the sample and the objective, then Equation 1 can be reformulated as:

$$w = \frac{2\lambda_{exc}}{\pi\,(n\cdot\sin(\theta))} = \frac{2\lambda_{exc}}{\pi\left(n\cdot\left(\text{height of incident } \frac{\text{beam}}{\text{focal}} \text{ length}\right)\right)} \quad \text{(Equation 2)}$$

Given a 488 nm excitation wavelength, a ~1 mm diameter beam, a 40 mm focal length illumination objective, and 1.33 refractive index of water, the beam waist is,

$$w = \frac{2\cdot 0.488}{\pi\left(1.33\cdot\frac{1.0}{40}\right)} = 9.322\ \mu m \quad \text{(Equation 3)}$$

Axial resolution and depth of field

The axial resolution of a microscope depends on the optical properties of the detection system and the refractive index of the sample. Considering the elongated shape of the intensity profile along the axial direction,[56] the theoretical axial resolution is the distance between the central maximum to the first minimum along the z axis:

$$z_{axial(th)} = \frac{2n\lambda}{NA^2} \quad \text{(Equation 4)}$$

where n is the refractive index of the sample, λ is the wavelength of the emitted light and NA is the numerical aperture of the imaging objective. With 510 nm peak emission wavelength of GCaMP6f, n = 1.38 for retina and 0.45 NA of imaging objective, the theoretical axial resolution is estimated as 6.95 μ m. The theoretical depth of field (DOF) is half the axial resolution:

$$DOF_{axial(th)} = \frac{n\lambda}{NA^2} \quad \text{(Equation 5)}$$

which is equal to 3.48 μ m.

Notably, these calculations assume that the detected light is emitted by a point source. However, scattering would tend to increase the Z-range of excitation, effectively increasing the axial resolution. Given the retina's scattering coefficient, μ_s, the effective axial resolution is given by the convolution of the expanded profile of the light-sheet, the excitation point-spread function and the detection point-spread function. To first order, the point spread functions can be approximated by Gaussians, which yields the following equation for effective axial resolution:

$$f\left(z_{axial(eff)}\right) = \left(c_1 \cdot e^{-(z_0 - z)/\mu_s}\right) \cdot \left(c_2 \cdot e^{-(z_0 - z)^2/2 \cdot \sigma_2^2}\right) \cdot \left(c_3 \cdot e^{-(z_0 - z)^2/2 \cdot (2 \cdot z_{axial})^2}\right) \quad \text{(Equation 6)}$$

Here, z_0 defines the plane of light-sheet and σ_2 is the beam waist. This effective DOF, which is twice the $z_{axial(eff)}$, was measured in the retina to be ~22 μ m (Figure 1F).

Scattering of excitation light

The retina has a scattering coefficient of ~57 cm^{-1},[19] compared to ~0.003 cm^{-1} of water. This means that the excitation light will undergo significant scattering as it travels through the retina. A large fraction of the incident photons is absorbed by the GCaMP6f protein, while the remaining fraction is scattered above and below the plane of excitation. The light scattered above the excitation plane can potentially reach the photoreceptors and activate them,[24] thereby producing visual responses independent of the stimulus.

To determine the degree of photoreceptor activation from scattered excitation light, we measured the total power of scattered light in the retina of an Ai148; PVCre mouse. Since scattered photons can travel along different directions, only a fraction of the scattered light reaches the photoreceptors. Therefore, to measure the intensity of scattered light that could activate photoreceptors, we used an aperture ~2 mm × 2 mm roughly matching the size of the imaged retina (Figure S1 a, b insets). The intensity of scattered light was converted to photoisomerization (P*) rate per cone expressing M− or S-opsin, and per rod, using Baylor and Govardovskii nomograms.[57,58] At ~3 mW laser power delivered at 488 nm to the retina in a typical experiment, the scattered excitation light produced ~10^4 P*/M-cone/s (Figure S1a), ~10^4 P*/rod/s and 10 P*/S-cone/s (Figure 2C). Since the UV stimulus produces ~10^5 P*/S-cone/s, the activation of S-cones from scattered excitation light is ~4 orders of magnitude lower than the photoisomerization rate produced by photopic UV stimulus[24] used in our experiments (Figure S1b).

Depth of field of imaging

Diffraction-limited point objects such as fluorescent beads are commonly used for assessing the spatial resolution of a microscope.[18] We used 500 nm diameter fluorescent beads coated with green-fluorescent dye embedded in 2% agarose gel (Figure 1C top) for measuring the depth of field. Images were acquired every 1 μm along the z-axis, while keeping the z-position of the sample and the excitation light-sheet unchanged. The (x, y) location of a bead was determined from the image with the bead in focus, and intensity was averaged over pixels within 1 standard deviation around the peak centered at (x, y). Using images at different z-positions, an intensity profile of the bead was measured as a function of the axial distance (Figure 1D). Since the detection objective collects more light from below the focal plane than above it, it leads to an asymmetrical intensity profile. Therefore, we symmetrized the intensity profile by reflecting the intensity curve about the excitation plane. By fitting a Gaussian function to the intensity profile and determining the full-width half maximum (FWHM) of the fit, we estimated the depth of field to be 8.5 ± 2.8 μm, averaged over n = 63 beads (Figure 1D inset).

Active ROIs, calcium responses and inferred spikes

To eliminate noisy, out-of-focus structures near the boundary of the imaged retina, a rectangular area containing the active ROIs was selected. Non-uniform illumination was corrected by homomorphic filtering and stripe artifacts caused by scattering of excitation beam were removed by spatial high pass filtering. Size of a template ROI was determined by first manually selecting contours around active somas (for RGCs) or active synapses (for BCs), and then estimating a mean radius from the ellipses fitted to the selected ROIs. The images were denoised by a Kalman Filter and were batch processed using the CNMF-E algorithm[27] to extract the time-varying fluorescence traces,

$$F_j(t) = A^{-1}\left(Y_j(t) - B_{0j} - B_j(t) - N_j(t)\right) \quad \text{(Equation 7)}$$

where j corresponds to the ROI index, $F_j(t)$ is the time varying fluorescent trace, A is the spatial matrix, $Y_j(t)$ is the raw trace, B_{0j} is the constant background, $B_j(t)$ is the time varying background and $N_j(t)$ is the time-varying noise. Manual verification was performed to remove overlapping ROIs and false positives. Steady drift in baseline fluorescence was corrected by subtracting the rolling 10^{th} quantile over a local time window from the raw trace. An estimate of $\Delta F(t)/F_0$ were obtained from the fluorescent trace prior to subtracting the baseline. The peak signal to noise ratio is given by the ratio of the average peak fluorescence of calcium transients to the standard deviation of the drift-subtracted baseline fluorescence:

$$SNR_{peak} = \frac{\langle F_{peak}(t)\rangle}{\langle N(t)\rangle} \quad \text{(Equation 8)}$$

To infer spikes from temporal fluorescent traces, the calcium transients were first fit using an autoregressive model of order 1. The modeled transients were then deconvolved from the fluorescent trace to estimate spike count $s_j(t)$:

$$s_j(t) = F_j(t) - k_{1j}F_j(t) \quad \text{(Equation 9)}$$

where, j corresponds to the j'th ROI, and k_{1j} corresponds to the first coefficient of the autoregressive model for the j'th ROI.

Response clustering and RGC classification

To cluster RGCs into different groups, trial-averaged responses to the chirp stimulus were used. Principal components were calculated using the full ensemble of trial-averaged responses. The responses of each RGC were then projected onto the leading principal components that accounted for at least 80% of the variance (Figure 3C). A Gaussian mixture model (GMM) with expectation maximization algorithm was fit to the projection values in the N-dimensional hyperspace with a pre-defined number of clusters determined from cross-validated Silhouette optimality test and Bayesian Information Criterion (BIC).[59] Response clustering was tested with alternative methods: Hierarchical agglomerative clustering (HAC) and Spectral clustering (SC). (Figure S2). Since each functionally distinct RGC type tiles the retinal space,[30] the conformity ratio[31] was computed for each cluster of RGCs (Figures 3G and 3H). Spike counts were obtained by the method described above (Equation 9), and the number of spikes corresponding to the count was uniformly distributed across the bin to obtain spike times.

Optimality and accuracy of clustering

To determine the quality of GMM fit to the projection values, we estimated Bayesian Information Criterion (BIC) values for different cluster sizes. The BIC value is defined as:

$$BIC(k) = -2\ln(L) + k\ln(n) \quad \text{(Equation 10)}$$

L is the maximum of Bayes likelihood, k is the number of estimated clusters and n is the number neurons. Since HAC and SC do not rely on model fits, optimality of cluster size was assessed by estimating the Silhouette coefficient for different cluster sizes using different clustering methods. For each cluster size, the Silhouette coefficient $S(i)$ for the i'th point in a cluster was calculated as:

$$S(i) = \frac{b(i) - a(i)}{\max\,(a(i), b(i))} \quad \text{(Equation 11)}$$

where, $a(i)$ is the mean distance from the i'th point to all other points in the cluster and $b(i)$ is the minimum of all distances from the i'th point to all other points in all other clusters. Normalized peri-stimulus time histograms of fluorescent traces were used for clustering and Silhouette coefficients were calculated for n = 100 iterations for each cluster size. The cluster size with the highest ratio of median and median absolute deviation was chosen as optimal (Figure S2). For GMM, both the Silhouette coefficient and Bayesian Information Criterion for model fits were used to cross-validate the optimal cluster size.

To determine clustering accuracy, responses were first clustered using three different clustering methods: GMM, HAC and SC, using a pre-defined cluster size. The median population temporal response for each cluster was then used to calculate pairwise correlation between responses, for each clustering method. Groups from each clustering method, with the highest pairwise response correlation, were assigned to the same functional type. The nearest-neighbor distances between RGCs for each group were assayed to confirm that the RGCs belonged to a unique functional type.

Quantification of stimulus preference

Directional preference was quantified by the direction-selective index (DSI):

$$DSI = \frac{\left|\sum R(\theta_j)e^{i\theta_j}\right|}{\sum\left|R(\theta_j)\right|} = \frac{\left|\sum\left(\int F_{\theta_j}(t)dt\right)e^{i\theta_j}\right|}{\sum\left|\int F_{\theta_j}(t)dt\right|} \quad \text{(Equation 12)}$$

where $R(\theta_j)$ corresponds to the area under calcium fluorescence response curve ($F_{\theta_j}(t)$) for a 100% contrast bright bar on a dark background moving along the direction θ_j. RGCs with DSI>0.3 were selected as DS-RGCs.[37] ON-OFF DS-RGCs were identified by two response peaks, corresponding to the ON and OFF responses to the entry and exit of the bar over the receptive field (Figure 4B).

Orientation preference was quantified by the orientation-selective index (OSI):

$$OSI = \frac{\left|\sum R(\theta_j)e^{2i\theta_j}\right|}{\sum\left|\sum R(\theta_j)\right|} = \frac{\left|\sum\left(\int F_{\theta_j}(t)dt\right)e^{2i\theta_j}\right|}{\sum\left|\int F_{\theta_j}(t)dt\right|} \quad \text{(Equation 13)}$$

where $R(\theta_j)$ corresponds to the area under calcium fluorescence response curve ($F_{\theta_j}(t)$) for a 100% contrast grating oriented along θ_j. All the RGCs with OSI>0.3 and DSI<0.3 were selected as OS-RGCs.[37] The grating moved in 12 directions at a speed of 24 μm/sec, repeated 5 times.

Receptive field estimation

Black and white checkerboard patterns with checker size ranging between 15 and 50 μm, refreshing at 60 Hz, were used to characterize spatiotemporal receptive field (RF) of RGCs. Temporal calcium traces were low pass filtered, and then spikes were inferred using methods described above (Equation 9). The sequence of checkerboard images $I(x, y)$ preceding each spike $s(t_j)$ was weighted by the inferred spike count and averaged over the number of spike events to obtain the spatiotemporal RF.

$$RF(x,y,\tau) = \frac{1}{N}\sum_{j=1}^{N} s(t_j)\cdot I(x,y,t_j+\tau) \quad \text{(Equation 14)}$$

Here, N is the total number of spikes and τ is the time lag between a spike and a preceding image.

Calcium transients have a decay time of 300–400 ms[7], therefore images presented over a 300 ms window preceding a spike event (i.e., τ <0.3 s), were used for estimating the temporal RF. The mean spatial image at each time lag was spatially filtered with a Gaussian of standard deviation 25 μm. The pixel values from the spatially filtered image within a 300 μm window centered around the RGC soma: (c_x, c_y) were averaged at each time lag to obtain the temporal RF.

$$RF(\tau) = \frac{1}{J\cdot K}\sum_{x=c_x-J/2, y=c_y-K/2}^{J/2, K/2} RF(x-c_x, y-c_y, \tau) \quad \text{(Equation 15)}$$

The temporal RF was fit with a parametric function $g(t)$

$$g(t) = a_1\left(\frac{t}{b_1}\right)^{c_1}\cdot e^{-\left(\frac{c_1\cdot t}{b_1}\right)} + a_2\left(\frac{t}{b_2}\right)^{c_2}\cdot e^{-\left(\frac{c_2\cdot t}{b_2}\right)} \quad \text{(Equation 16)}$$

and the mean image corresponding to the closest peak (for ON RGC) or trough (for OFF RGC) to the spike event was used as the representative 2D spatial RF. The RF center was fitted with a two-dimensional Gaussian with 1 SD boundary around the center maximum or minimum.

BC response characterization

For extracting the ROIs for each release site, the following threshold values were used: (1) peak signal to noise ratio (SNR_{peak}) = 2, (2) spatiotemporal pixel intensity correlation = 0.7, and (3) ROI template diameter = 1–4 μm. After ROI extraction, duplicate and overlapping ROIs were manually removed. Fluorescence transients associated with the spot stimulus were identified by using a threshold value 5 times the median absolute deviation (MAD) of the entire temporal response. The peak signal to noise ratio, rise time, and decay time were used to characterize the kinetics of the response transients. The time for a transient response to rise to its peak value from baseline was considered as the rise time. The time constant of decay was obtained from an exponential fit to the response curve within a 4 s window following the response peak. Positive (negative) contrast preference was determined by an increase followed by a decrease in calcium fluorescence to the appearance followed by disappearance of a bright (dark) spot (Figure 5).

Statistical analysis

Statistical analyses of data were done using custom scripts written in MATLAB (Mathworks, Natick, MA) and CAIMAN analysis codebase.[27] Summary data are presented as mean ± SEM (Standard Error or Mean), mean ± SD (Standard Deviation), median ± MAD (Median Absolute Deviation), as noted in figure legends or text. Statistical significance was determined from p-values, for parametric test (Student's t test) or non-parametric test (two-sided Wilcoxon rank-sum test), with appropriate corrections for multiple samples of different sizes. Optimality and reliability of clustering were determined using K-means distance, Silhouette Coefficient and Bayesian Information Criterion.